

DESIGN AND PERFORMANCE OF A MICROCHANNEL SUPERCRITICAL CARBON DIOXIDE RECUPERATOR WITH INTEGRATED HEADER ARCHITECTURE

Cameron Naderi,¹ Erfan Rasouli,² Vinod Narayanan,^{3,*} & Christian Horend⁴

¹Murray Company, San Leandro, California, USA

²Western Cooling Efficiency Center, University of California, Davis, California, USA

³Department of Mechanical and Aerospace Engineering, University of California, Davis, California, USA

⁴RWTH Aachen University, 52056 Aachen, Germany

*Address all correspondence to: Vinod Narayanan, Department of Mechanical and Aerospace Engineering, University of California, Davis, California 95616, USA; Tel.: +1 530 752 9086, E-mail: vnarayanan@ucdavis.edu

Original Manuscript Submitted: 8/10/2018; Final Draft Received: 12/31/2018

Supercritical carbon dioxide (sCO₂) power cycles have gained attention due to the relatively high efficiency and potential for simple controls. Because the temperature drop across the turbine is fairly low in sCO₂ cycles, heat recuperation is key to high cycle efficiency. In this paper, an integrated header microchannel (IHM) recuperator design is proposed for the sCO₂ power cycle. The recuperator consists of multiple short unit cells connected together by a series of flow headers to inlet and exit plena. Within each unit cell, sCO₂ flows through a microscale pin-fin array on the hot and cold sides. The thermal-fluidic performance of a representative three-layered unit cell stack is experimentally characterized. Three-dimensional computational fluid dynamics and structural analysis simulations are performed to develop the unit cell design. Experimental results indicate that effectiveness in the range of 84–95% can be achieved for a unit cell length of 18 cm and a heat capacity rate ratio ranging from 0.35 to 1. The experimentally determined overall heat transfer coefficient and pressure drop are compared against correlations in literature. The Prasher et al. [J. Heat Transfer, vol. 129, no. 2, pp. 141–153, 2007] correlation predicts the experimental pressure drop to within 9%. No heat transfer correlation was found to predict the experimental data well, with the Rasouli et al. [Int. J. Heat Mass Transfer, vol. 118, pp. 416–428, 2018] correlation showing the lowest mean average error of 29%. A heat exchanger model is developed based on the Prasher et al. and Rasouli et al. correlations. The model is integrated within a single recuperator sCO₂ cycle model to assess the impact of the IHM recuperator on the cycle efficiency.

KEY WORDS: microchannel recuperator, printed circuit heat exchangers, supercritical carbon dioxide power cycle, recuperator, effectiveness, cycle performance, microscale pin fins

NOMENCLATURE

A	surface area for heat exchange (m^2)	$\text{Re}_{A_{\min}}$	Reynolds number based on $D_{A_{\min}}$, $= \rho U_{\max} D_{A_{\min}} / \mu$
A_{\min}	minimum flow area within the pin fin array (m^2)	Re_{D_h}	Reynolds number based on D_h
C	heat capacity rate (W/K)	S_D	diagonal pitch (m)
C_r	heat capacity rate ratio ($= C_{\min} / C_{\max}$)	S_L	longitudinal pitch (m)
D	circular pin-fin diameter (m)	S_T	transverse pitch (m)
D_h	channel hydraulic diameter (m) hydraulic diameter based on pin-fin size (m)	T	temperature ($^{\circ}\text{C}$)
$D_{A_{\min}}$	hydraulic diameter calculated based on A_{\min} and P_{\min} (m)	t_d	diffusion time (s)
f	Darcy friction factor, $= \Delta P / [(1/2) \rho U_{\max}^2] N_{\text{row}}$	t_{res}	resident time (s)
h	enthalpy (J/kg)	t_{wall}	wall thickness (m)
H	height (m)	u_m	mean velocity through channel (m/s)
htc	heat transfer coefficient ($\text{W/m}^2 \cdot \text{K}$)	U	overall heat transfer coefficient ($\text{W/m}^2 \cdot \text{K}$)
k	thermal conductivity ($\text{W/m} \cdot \text{K}$)	U_{\max}	maximum velocity across pin fin array (m/s)
L	length (m)	V	volume (m^3)
MAE	mean absolute error, $= (1/N) \sum_1^N (\phi_{\text{exp}} - \phi_{\text{pred}} / \phi_{\text{exp}}) \times 100\%$	W	width (m)
\dot{m}	mass flow rate (kg/s)	Greek Symbols	
N_{row}	number of pin-fin rows in flow direction	α	heat or species diffusivity (m^2/s)
N_{stack}	number of stacks of unit cells	β_L	longitudinal pitch ratio, $= S_L / D_h$
NTU	number of transfer units	β_T	transverse pitch ratio, $= S_T / D_h$
$\text{Nu}_{A_{\min}}$	average Nusselt number calculated based on $D_{A_{\min}}$, $= \text{htc} D_{A_{\min}} / k$	ε	effectiveness
Nu_{D_h}	average Nusselt number calculated based on D_h	Φ	unspecified term
P	pressure (Pa) or (bar)	μ	viscosity (Pa.s)
P_{\min}	wetted perimeter associated with A_{\min} (m)	ρ	density (kg/m^3)
ΔP	pressure drop (Pa) or (bar)	η	cycle efficiency
Pr	Prandtl number	Subscripts	
q	heat transfer rate (W)	c	pertains to cold side
		exp	experimental value
		h	pertains to hot side
		i	at the inlet

NOMENCLATURE (*continued*)

IHM	integrated header microchannel	<i>o</i>	at the outlet
lm	log mean	pin	pertains to a pin
loss	loss	pred	predicted value
max	maximum	recup	recuperator
min	minimum	unit cell	pertains to unit cell
mod	modified	wall	calculated at the wall

1. INTRODUCTION

The supercritical carbon dioxide (sCO₂) Brayton cycle has garnered a great deal of attention in recent years due to high ideal cycle efficiency (in excess of 50%) at moderate fluid temperatures ranging from 550 to 800°C. Advantages include compactness of turbomachinery, simpler controls, and high efficiency at moderate temperatures. Several research groups are investigating use of this power cycle with varied sources such as fossil, solar, nuclear, geothermal, and moderate-to high-quality waste heat streams (Brun et al., 2017; Ahn et al., 2015; Irwin and Moullec, 2017; Turchi et al., 2013).

Because the temperature drop across the turbine is fairly low in sCO₂ cycles, high-effectiveness heat recuperation is key to high cycle efficiency. An impediment to obtaining high effectiveness is that the approach temperatures of the fluid streams are low and hence these recuperators tend to be large. To increase the cycle efficiency, variants of a single recuperator cycle such as the recompression cycle have been proposed. In such cycles, the high-temperature recuperator would need to be fabricated using expensive nickel superalloys when the turbine inlet temperature is 800°C or higher. Hence, it is important to reduce the size of the recuperator from a cost perspective. The motivation behind this work is to develop a high-effectiveness, compact recuperator using microchannel technology.

Microchannels are used for enhancing heat and/or mass transport in diffusion-limited conditions (Narayanan et al., 2013; Kockmann, 2008). For laminar flows, the time for heat diffusion scales as the square of the channel hydraulic diameter, $t_d \propto D_h^2/\alpha$, where α is the thermal diffusivity. Heat transfer can occur from the fluid to the walls of the channel as long as the residence time of the fluid within the channel, $t_{res} \propto L/u_m$, is on the order of the diffusion time, t_d . Therefore, the required channel length, L , can be as small as $L \propto (D_h^2 u_m)/\alpha$, thereby enabling compact devices. Over the past three decades, a significant body of literature has emerged on fundamental thermal-fluidic aspects of microchannels. Microchannels have been used in several applications such as heat sink thermal management (Tuckerman and Pease, 1981; Narayanan et al., 2013), compact heat and mass exchangers (Brandner et al., 2017; Kockmann, 2008), and chemical reactors (Karagiannidis and Mantzaras, 2010; Tonkovich et al., 2004).

In the context of recuperators for nuclear reactors and sCO₂ power cycles, compact heat exchangers have been designed by companies like Heatric and others (Le Pierres et al., 2011; Li et al., 2006, 2008; Mylavarapu et al., 2012; Kim and No, 2011; Carlson et al., 2014; Chen et al., 2016). These “printed circuit heat exchangers” (PCHes) are fabricated by photochemical machining (etching) and diffusion bonding plates, or shims, of metal. The channels are etched

into the plates and are about 1 mm in width and 0.5 mm in depth and are typically either straight, zig-zag, or curved in design. The plates could be as large as 150 cm long by 60 cm in width, depending on the rating of the PCHE and the manufacturing limitations. The diffusion bonded stack forms a heat exchanger core onto which large headers are welded. The surface-to-volume ratios of these PCHEs are large, in the range of $650 \text{ m}^2/\text{m}^3$, making them an attractive option for sCO_2 recuperators.

Over the past few years several groups have characterized heat exchange performance of PCHE-type recuperators for sCO_2 power cycle experimentally and computationally. Nikitin et al. (2006) experimentally characterized the thermo-hydraulic performance of a Heatric zig-zag PCHE developed for sCO_2 refrigerators and heat pumps. The pressures ranged from 65 to 105 bar and 22 to 32 bar, and temperatures ranged from 280 to 320°C and $90\text{--}108^\circ\text{C}$ on the cold and hot sides, respectively. For a hot side Reynolds number in the range of 2750–6000, the overall heat transfer coefficient was found to be in the range of $300\text{--}625 \text{ W/m}^2\text{-K}$. Effectiveness as high as 99% was observed.

Tsuzuki et al. (2007) proposed a discontinuous S-shaped fin and compared its performance to the traditional zig-zag channel PCHE using computational fluid dynamics (CFD) simulations. They found that under identical heat transfer performance, the pressure drop of the new S-shaped channel design was only 1/5 that of the zig-zag channel. In a follow-up study, Ngo et al. (2007) experimentally compared the performance of a zig-zag PCHE and an S-shaped fin PCHE. The configuration tested had 8 hot-side channel plates and 4 cold-side channel plates; two hot-side plates were stacked together and surrounded by the cold plates. The results showed that while the pressure drop of the zig-zag channels were larger than the S-shaped channel by 4–5 times in the range of flow tested, the Nusselt number was 24–34% larger as well. Overall heat transfer coefficients in the range of $250\text{--}700 \text{ W/m}^2\text{-K}$ were obtained for the S-shaped fin PCHE over a Reynolds number range of 3000 to 20,000.

Fourspring et al. (2014) experimentally characterized two novel designs for the sCO_2 recuperator developed by Brayton Energy. The first design consisted of folded wavy fins on both the hot and cold sides brazed to form flow passages. A surface area to volume ratio of $4000\text{--}5000 \text{ m}^2/\text{m}^3$ was achieved using this method. The second design used wire mesh in the hot and cold flow paths and resulted in a heat transfer area to volume ratio of $7000\text{--}8000 \text{ m}^2/\text{m}^3$. Average effectiveness of 0.80 was obtained in the experimental measurements on the wavy fin design and the measured pressure drop was less than one-half of the design pressure drop at 200 kW. However, the wire mesh recuperator resulted in a very large pressure drop.

Meshram et al. (2016) compared the performance of straight and zig-zag channel PCHE using CFD simulations in turbulent flow conditions. They simulated a single hot and cold layer of the PCHE and varied the channel hydraulic diameter and flow Reynolds number. They developed correlations for Nusselt number and friction factor from the simulations and used these in a one-dimensional heat exchanger model for the PCHE. They found that the zig-zag channel PCHE was significantly smaller than the straight-channel PCHE but with the downside of a significantly higher pressure drop. They suggested that a cycle analysis would be needed to be performed to determine the impact of using a compact PCHE.

2. MOTIVATION AND OBJECTIVES

Studies in literature on PCHE recuperators demonstrate that this type of heat exchanger is suitable for sCO_2 cycles. However, there is room for improvement of size by going to smaller channel dimensions in the 100–300 micrometer range since, as discussed above, the channel length

scales directly with the square of the channel hydraulic diameter. Since pressure drop would be large for these small channel dimensions, it is imperative that a different type of flow distribution header architecture be used with the shorter and smaller diameter channels.

In this paper, a different microscale architecture for the sCO₂ recuperator is presented using the principles of scaling afforded in microscale devices. This approach involves short heat exchange channels or “unit cells” where heat exchange occurs. The unit cells are connected together using headers integrated with the unit cells. The capacity of the recuperator is obtained through “numbering up” of the unit cells. A key advantage of such an architecture lies in reduced size for the same heat exchange rate or pressure drop when compared to the PCHE designs. Additionally, a pin fin architecture as opposed to straight or zig-zag design is used in the unit cells. The overall design of an integrated header microchannel (IHM) recuperator is first discussed. Design of a small-scale three-pair unit cell stack recuperator is then discussed. Thermo-hydraulic experiments on the unit cell are then described. The experimental results are used to validate correlations of pressure drop and heat transfer coefficient used in a heat exchanger model to predict the IHM recuperator performance. Lastly, the IHM recuperator model is incorporated into a single recuperator cycle model to determine the effect of the IHM recuperator performance on the cycle efficiency.

3. IHM RECUPERATOR DESIGN

A solid model of the IHM recuperator model is shown in Fig. 1(a), and a cut-away view along the plane indicated in Fig. 1(a) is shown in Fig. 1(b). Example inlet and outlet temperatures corresponding to a single recuperator sCO₂ cycle are shown in Fig. 1(b). The red and blue arrows indicate flow paths of the hot and cold fluids, respectively, within the IHM recuperator.

The building blocks of the IHM consist of pairs of hot and cold microscale fluidic passages through pin arrays. A pin-fin architecture [Fig. 1(f)] is used for the microscale regions since it lends to higher heat transfer rate and better flow distribution compared with parallel microchannel arrays (Tuckerman, 1984; Peles et al., 2005). A pair of hot and cold pin arrays forms a “unit cell.” These pairs are arranged vertically to form a “unit cell stack” (UCS) as shown in Fig. 1(e).

Circular headers bring hot and cold fluid in and out of the unit cells in the stack as shown in Fig. 1(d). These headers are connected to secondary UCS plena on the top and bottom of the UCS in Fig. 1(d). The UCS plena feed into the IHM headers as shown in Fig. 1(b). The UCS stacks integrated with UCS plena can be treated as a modular unit that can be replicated laterally to increase the capacity rating of the IHM, as shown in Figs. 1(c) and 1(b). The rating can also be increased by increasing the number of unit cells stacked vertically within each UCS.

In order to permit exchange of heat in the UCS and IHM plena, hot and cold fluid plena are located adjacent to each other. The hot fluid inlet plenum is located adjacent to the cold fluid outlet plenum while the hot fluid exit plenum is located adjacent to the cold fluid inlet plenum. Additionally, the plena with the lower temperatures (cold fluid inlet and outlet plena) are located at the periphery of the IHM recuperator to reduce heat loss to the ambient.

4. UNIT CELL STACK (UCS) EXPERIMENTS

To validate the performance of the IHM recuperator described above, detailed design of a unit cell was undertaken. A UCS consisting of three layers connected by circular headers was then fabricated and experimentally characterized. A microlamination approach consisting of chemical etching and diffusion bonding was used to fabricate the UCS. The material used was stainless

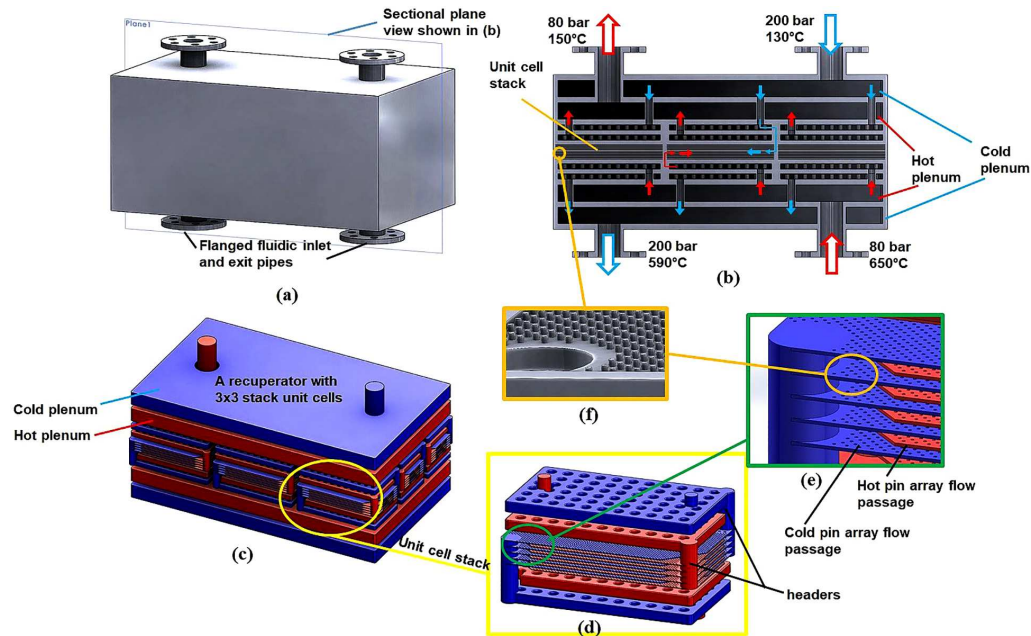


FIG. 1: IHM recuperator concept. (a) Solid body model of the IHM recuperator with four flanged fluidic inlets and exits. (b) Sectional view of plane shown in (a) showing the cold and hot fluidic paths within the IHM recuperator. The fluids cascade through two levels of plena, namely the outer IHM plenum and the inner UCS plenum before entering the microchannel UCS. (c) Fluid volume within the IHM recuperator shown in (a). The IHM shown in this figure has nine unit cell stacks arranged in a 3×3 pattern. (d) Detail of the secondary UCS plenum and a UCS within the IHM recuperator. The unit cell stack shown here consists of five pairs of unit cells. (e) Detail of the fluid volume within the unit cell stack showing hot and cold arrays of microscale pin arrays connected by circular headers to the secondary plenum. (f) Detailed solid model of the microscale pin array and header.

steel 316. Since the differential pressure between the hot and cold layers is about 100 bar, a mechanical design of the layers was needed. The design process was iterative between fluid flow and structural analysis.

4.1 Design and Fabrication of Unit Cell

The pin array on the layers was patterned using chemical etching. Due to the limitations of chemical etching, for a given pin height, the closest edge-to-edge distance of the pins from one another is equal to twice the depth of the cut. Pin height was chosen based on a balance between low pressure drop (with higher aspect ratio pins) and the degradation of pin-fin efficiency with fin height. To fabricate the pin array, half of the pin depth was etched onto two opposing shim faces to acquire the desired height. The low aspect ratio of the design, caused by the limitation of the chemical etching method, precluded existence of vortex shedding in the pin array (Rasouli et al., 2018). Such vortex shedding, observed in the wake of the pins of higher aspect and pitch ratios by Rasouli et al. (2018), can lead to increased heat transfer coefficient. Other fabrication designs, such as wire electric discharge machining, could be used in the future to generate higher aspect ratio designs.

The pitch between the pins was decided through the structural analysis (see Naderi, 2017, for details). A staggered pin arrangement was chosen due to its superior heat transfer characteristics compared to an in-line pattern. The spacing of the staggered pattern was chosen to be an equilateral arrangement, which would make the stress distribution more uniform. The chemically etched plates were first characterized and then diffusion bonded. The design dimensions of the pin were chosen to be 700 μm and 500 μm , respectively, for diameter and height. The transverse pitch, S_T , was 1200 μm while the longitudinal pitch, S_L , was 1040 μm . Figure 2(a) shows an optical microscope top-view detail of the pin array with the nomenclature and dimensions noted. To characterize pin diameter and spacing, images of several locations across different shims were obtained using an AmScope digital camera mounted on an Olympus microscope. Parameters of interest were then measured using AmScope software that had been calibrated with an optical calibration grid (Edmund 1951 USAF Glass Slide Resolution Target). Measurements of pin height were performed using a confocal microscope [Fig. 2(b)]. Table 1 shows the comparison of the design values and the fabricated dimensions. As can be seen from the measurement results, average values for D , S_T , S_L , and pin depth H_{pin} were all within at most 3% of the nominal value. While this variation did not affect the viability of using the shims, additional

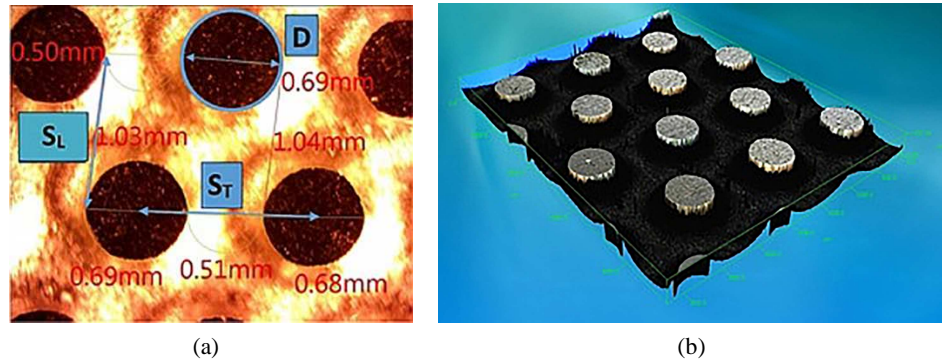


FIG. 2: Characterization of pin array dimensions. (a) Sample micrograph taken using AmScope microscope digital camera. Flow would be directed from the bottom to top. Characterized parameters are denoted in the figure. (b) Digital image created by Zeiss CSM 700 confocal microscope.

TABLE 1: Measured and nominal values for pin diameter and spacing of the pin array

—	MEASURED AVERAGE	NOMINAL VALUE
D (μm)	682 ± 3	700
S_T (μm)	1186 ± 3	1200
S_L (μm)	1054 ± 23	1040
$(1/2) H^\dagger$ (μm)	250 ± 5.3	250
H/D	—	0.71
S_T/D	—	1.7
S_L/D	—	1.5

[†]This height is one-half the total height of the pin, since two etched layers are bonded together.

mechanical analysis with the updated parameters was conducted to confirm the structural integrity of the recuperator.

An exploded view of the UCS is shown in Fig. 3. Three hot and cold layers of pin-fin arrays were arranged in a counter-flow configuration, similar to that seen in typical plate-type heat exchangers. The inlet and exit pathway headers were laser cut into the layers. Each layer was 1 mm in thickness and consisted of 250 μm etched pin arrays on both sides. The length of the UCS was 18 cm and the width was 2.5 cm. The calculated area density based on surface area for heat exchange to the total volume was $1500 \text{ m}^2/\text{m}^3$. The outer layers of the UCS were made 3 mm in thickness to accommodate the large pressure differential of 200 bar between the internal flow and the ambient. The entire thickness of the UCS was 11 mm.

Structural analysis was accomplished using ANSYS Mechanical APDL on two different domains shown in Fig. 3. The computational domain of the shims included only the portion of the shims closest to the headers due to negligible stress concentrations elsewhere along the length of the pin array. The first domain comprised shims that formed an inner unit cell of the heat exchanger; such sections were only exposed to atmospheric pressure around their perimeters. The second domain represents a channel at the top and bottom of the heat exchanger that are fully exposed to the atmosphere. Faces on the top, bottom, and side cross-sectional walls, along with the cut face of the pins, were all assumed to be symmetrical in the simulations. The inner channels in both test sections were simulated at a pressure of 200 bar while the outer channels were simulated at 100 bar. Additionally, atmospheric walls were subjected to 1 bar of pressure. The material used in the simulations is stainless steel 316 which exhibits a yield strength of $\sim 200 \text{ MPa}$ at 400°C (AISI, 2018). Note that when used in the sCO_2 recompression power cycle, the temperatures experienced by the high-temperature recuperator would be on the order of 550°C , necessitating the use of nickel superalloys for fabrication. SS316 was used instead

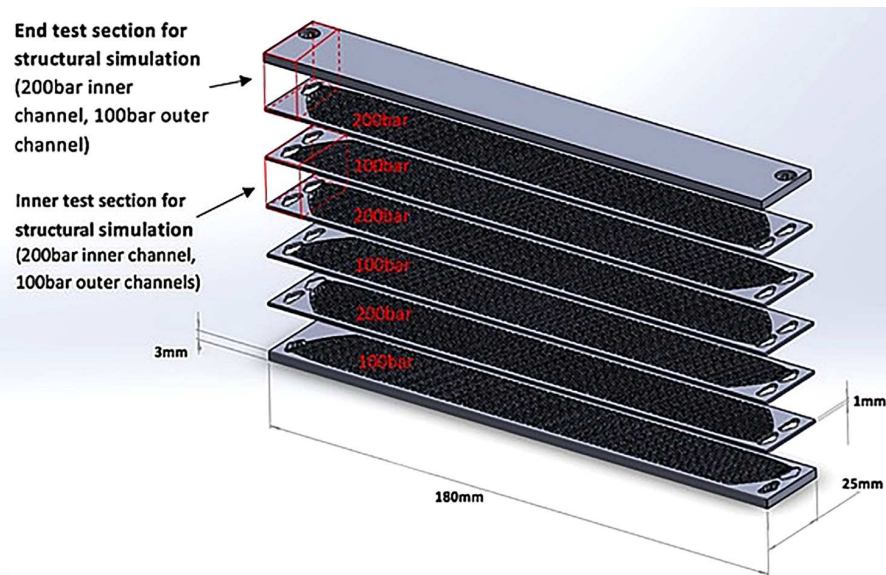


FIG. 3: Exploded view of UCS showing the overall device dimensions. The two regions in the top left are domains of interest for the mechanical stress simulations. Pressures of the fluid within each layer are also identified.

due to ease of fabrication and pressure and temperature limitations of test facility. Mechanical stress simulation results showed a maximum stress of 83 MPa in the inner domain of the heat exchanger and 129 MPa in the second domain, both of which fall below the yield strength of the material.

In conjunction with the mechanical stress analysis simulations, computational fluid dynamics (CFD) simulations were performed to determine the flow distribution within each layer. A single layer of fluid volume through the pin fin array was modeled using a commercial finite volume solver, ANSYS FLUENT v19. Figure 4(a) shows the fluid volume of the geometry that was simulated. The pin array dimensions are as shown in Table 1. In order to distribute flow from the inlet region through the width of the unit cell, a gradual tapered path from the inlet and to the exit, along with flow distribution structures (FDS) were added. The inset in Fig. 4(a) shows a detailed view of the tapered entrance of the pin array and the flow distribution structures. Using ANSYS Static Structural and FLUENT, an iterative process was used to find suitable spacing and orientation for the flow distribution structures.

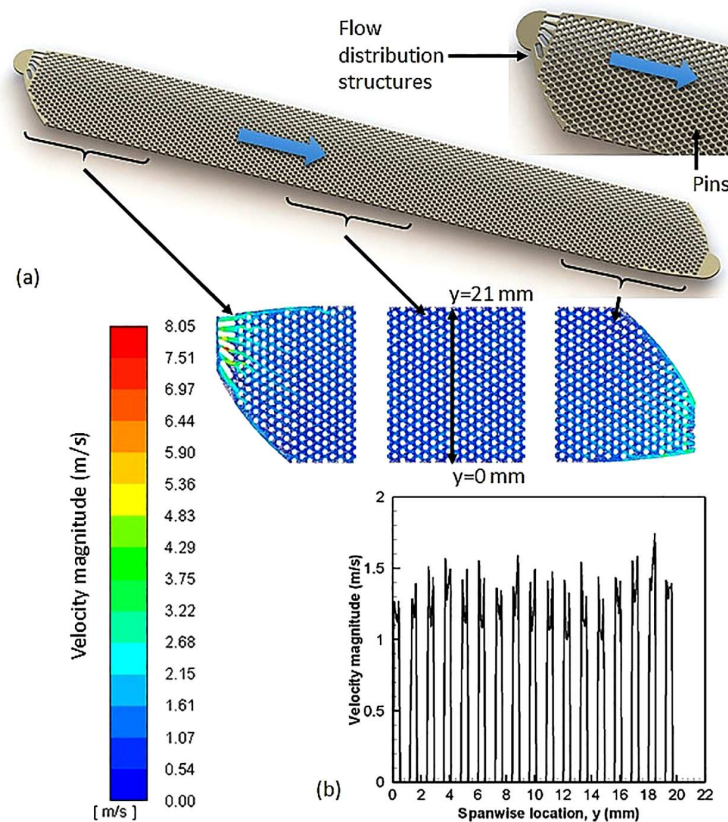


FIG. 4: (a) Fluid volume through the pin-fin array. The inset detail on the top shows details of the flow distribution structures that were designed to permit a uniform flow distribution across the width of the pin array. (b) (Top) Top view of velocity magnitude contour in a plane cutting through the middle of the flow channel at the inlet, middle, and exit sections. Black line in the middle section indicates location of raked line used for velocity measurement. (b) (Bottom) Plot of velocity magnitude at the center location indicated by the black line in the contour plot.

The mass flow rate through each layer of hot or cold fluids in the experiment was varied, but limited by the maximum mass flow rate of 1.7 g/s based on the pump limitations. Hence, the maximum flow rate through each layer was set at 0.29 g/s. A uniform velocity of 1.248 m/s, calculated using the area of the opening into the microchannel, mass flow rate, and fluid density, was applied at the inlet. Properties of carbon dioxide were estimated using Engineering Equation Solver (EES, F-Chart Inc.) at a pressure of 80 bar and an average temperature of 400°C. The outlet of the pin array was designated as a pressure outlet and no-slip conditions were applied to all walls.

The Reynolds number based on the pin diameter was 2,110. A k- ω Shear Stress Transport model was used to model turbulence in order to better predict flow separation in the wake of the pins. The geometry in Fig. 4(a) was meshed using ANSYS Meshing in ANSYS Fluent V19. The mesh size function was set to proximity and curvature, while the minimum mesh size and growth rate were adjusted to achieve different number of meshing element numbers. A grid independence study was performed with 11, 20, and 35 million elements. The difference in pressure drop between the 20 and 35 million element simulations was 1.9%. Hence, the 20 million element simulation was deemed satisfactory for the simulations used in the design of the recuperator and in pressure drop estimates. Results of the simulation are presented as a contour plot in Fig. 4(b). Regions of higher velocity are seen in the entrance in between the flow distribution structures and at the exit where the flow converges from the pin array to the header. A plot of the velocity magnitude at the mid-plane of the channel and across the pin array is shown in Fig. 4(b). Peak mid-plane velocity magnitude between the pins was found to be 1.49 m/s with a standard deviation of 0.11 m/s (7%). This deviation was deemed as an acceptable level of uniformity of the flow across the width of the channel and the pin array design shown in Fig. 4(a) was chosen for fabrication.

The chemically etched plates were diffusion bonded and tubes were brazed to the inlet and exits of the two fluid streams. Structural integrity was confirmed through a static pressure test at room temperature. The system was pressurized every 20 bar up to a maximum of 120 bar and held isolated from the pressure source for 20 min at the set pressure. No variation was observed in the pressure during the hold time.

4.2 Experimental Apparatus and Procedure

A schematic of the test facility is shown in Fig. 5. Carbon dioxide was provided by a source cylinder in a liquid phase at ~ 64 bar and 23°C. The fluid was filled into a 3.8 liter stainless steel cylindrical reservoir that was concentrically housed inside a clear PVC pipe that served as a cooling jacket. The jacket provided a constant flow of 5°C chilled water that surrounded the cylinder and cooled the CO₂ inside down to near 5°C. From the reservoir, the liquid CO₂ was sent to the HPLC pump where it was pressurized between 80 and 90 bar and pumped at the user-specified flow rate. The pressure data downstream of the pump were collected via a signal output by the pump, and a thermocouple was used to monitor the temperature of the CO₂ after the pump head. The line between the reservoir and pump also contained a pressure relief valve (PRV1) that was specified to relieve pressure in the line if the pressure in the reservoir exceeded 103 bar. While the UCS was designed for higher pressures, experiments were performed at less than 100 bar due to the pressure limit on the Coriolis mass flow meter.

Liquid CO₂ was then split into two streams. Needle valves NV1 and NV2 regulated the flow of each stream before they entered the hot oil bath. Coriolis mass flow meters (Micro Motion CMF010H Mass Flow Meter) were used to monitor the mass flow rate of each stream. The

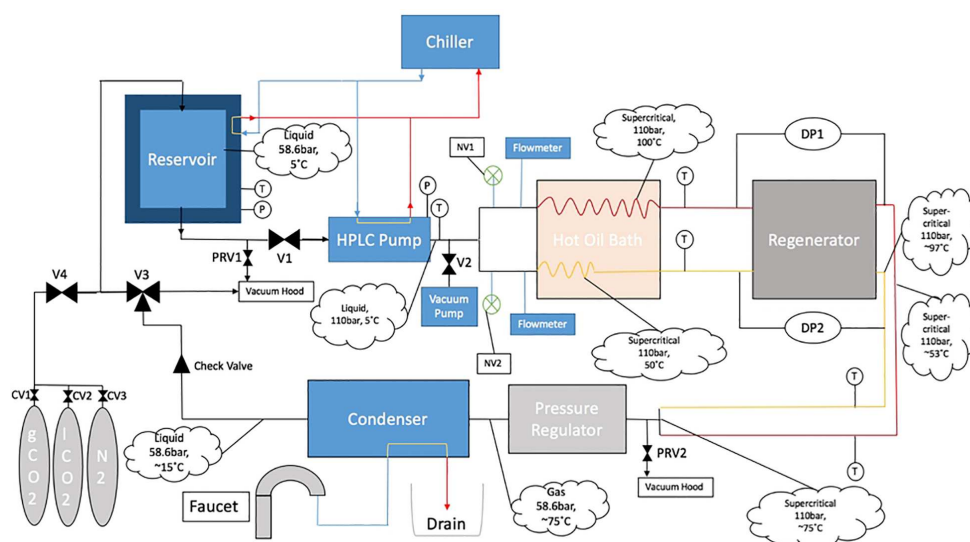


FIG. 5: Simplified schematic of the test loop. Captions indicate state of CO₂ at every major point along the loop.

streams then entered the hot oil bath, which was set to a user specified temperature. Differences in coil length for the two streams resulted in the temperature difference that defined the hot and cold streams entering the UCS. Temperatures at the outlet of the oil bath of each stream were also monitored. It was at this stage in the process, at the outlet of the hot oil bath, that the liquid CO₂ exceeded the 73.8 bar/31°C critical point and entered a supercritical state.

Upon heating CO₂ to a supercritical state, both streams entered the UCS. Temperatures of the inlet and outlet sides of both streams were recorded. The differential pressure across the hot and cold channels was also measured using Validyne DP15 differential pressure transducers.

Once the two streams exited the UCS, they were combined together and entered a forward pressure regulator. After being regulated down in pressure, the carbon dioxide went through a cooling coil that was submerged in a container of continuously refreshing tap water. Liquid carbon dioxide then exited the condenser and flowed through a check valve used to prevent potential issues with backflow in the system.

All sensors (namely thermocouples, gauge pressure transducers, differential pressure transducers, and flow meters) were connected to NI Data Acquisition modules. LabVIEW software was used for all signal processing and data collection. The range of varied parameters and their uncertainty are shown in Table 2. Uncertainties in estimated parameters, discussed in the next section, were evaluated using a propagation of errors method (Moffat, 1988), and are also shown in Table 2. Error in results was not found to be substantial and is not shown in the results plots for visual clarity.

4.3 Experimental Data Analysis

The raw data collected from testing were processed in order to characterize the performance of the UCS. Temperature and absolute pressure data were also used to compute density, dynamic viscosity, specific enthalpy, and specific heat of carbon dioxide.

TABLE 2: Parameter range and uncertainties in measured and determined variables

Measured Variable/Instrument	Instrument	Range	Uncertainty
Mass flow rate	Micro Motion™ Coriolis flowmeter	0.25–1.6 g/s	0.1% of flow rate
System pressure	Omega absolute pressure transducer	88–100 bar	0.25% of full scale
Hot inlet temperature	Type-T thermocouple	80–105°C	0.023°C
Cold inlet temperature	Type-T thermocouple	48–66°C	0.026°C
Hot outlet temperature	Type-T thermocouple	51–86°C	0.030°C
Cold outlet temperature	Type-T thermocouple	77–100°C	0.024°C
Pressure drop	Validyne™ capacitance transducers	1.7–9 kPa	0.03 kPa (low range), 0.04 kPa (mid range), and 0.05 kPa (high range)
Overall heat transfer coefficient, U	—	—	1.3%
Effectiveness, ϵ	—	—	0.15%
Number of transfer units, NTU	—	—	1.2%

Heat exchanger performance is typically presented as a plot of effectiveness against the Number of Transfer Units (NTU) for different values of heat capacity rate ratios, C_r . This ratio is defined as the ratio of the minimum heat capacity rate stream to the maximum heat capacity rate stream in the heat exchanger. Effectiveness, ϵ_{recup} , is calculated as the ratio of the transferred heat to the maximum possible heat transfer:

$$\epsilon_{\text{recup}} = q_c / q_{\text{max}} \quad (1)$$

The maximum possible heat transfer rate in Eq. (1) was estimated as

$$q_{\text{max}} = \dot{m}_{\text{min}} (h_{h,i} - h_{c,i}) \quad (2)$$

where \dot{m}_{min} denotes the minimum mass flow rate of the hot or cold streams in the heat exchanger and h denotes specific enthalpy (subscript denotes hot/cold stream and inlet/outlet). In Eq. (1), the heat transfer rate in the heat exchanger was determined using the heat rate gain by the cold side,

$$q_c = \dot{m}_c (h_{c,o} - h_{c,i}) \quad (3)$$

where \dot{m}_c denotes the mass flow rate of the cold side.

The specific enthalpy is used in defining q in Eqs. (2) and (3) to account for the potential for large variation in specific heat capacity with temperature for sCO₂. Over the range of experimental conditions, if the average specific heat capacity on hot and cold sides and fluid inlet and exit temperatures are used, the average and maximum differences were 3.8% and 16.5%, respectively.

The NTU of the recuperator is defined as

$$\text{NTU} = UA / C_{\text{min}} \quad (4)$$

where U is the overall heat transfer coefficient of the recuperator, and A is the surface area for heat exchange. The combined product of UA , known as the heat conductance, represents the inverse of the total resistance in the path for heat to be transferred from the hot to the cold fluid stream within the heat exchanger. The term C_{\min} denotes the smaller of the two heat capacity rates of the fluid streams within the device.

The NTU can be determined using Eq. (4) if the UA value was known. This value can be obtained using correlations or by computational simulations, by computing the resistances in the path for heat transfer. This UA value can also be determined experimentally by a measure of the heat transfer rate in the device and the inlet and exit temperatures of the fluid streams,

$$UA = q_c / T_{\text{lm}} \quad (5)$$

The log mean temperature (T_{lm}) in Eq. (5) is defined for a counter-flow heat exchanger as:

$$T_{\text{lm}} = [(T_{h,i} - T_{c,o}) - (T_{h,o} - T_{c,i})] / \ln \left(\frac{T_{h,i} - T_{c,o}}{T_{h,o} - T_{c,i}} \right) \quad (6)$$

The overall heat transfer coefficient U was determined based on the surface area of the hot side of the heat exchanger, A_h , which included the pin surface area.

In an ideal heat exchanger with no heat loss, the heat transfer rate from the hot side should be identical to the heat gained by the cold side [Eq. (3)] and either could be used in the numerator of Eq. (1) to estimate the effectiveness. However, in the experiments, despite thorough insulation with multiple layers of low-conductivity thermal insulation blanket, heat loss was observed from the difference between heat rates estimated on the hot and cold sides. In large-scale recuperators, the ratio of heat transfer area to heat loss area is large and hence the ratio of heat loss to heat exchange is small. However, since the UCS has only three pairs of heat exchange surfaces, the surface area for heat loss was of the same order as the heat exchange area, and hence a heat loss correction was warranted. Nikitin et al. (2006) also found that it was important to account for heat losses for such small laboratory-scale PCHEs despite thorough insulation.

In order to quantify the heat loss from the UCS, a heat loss calibration experiment was performed. In the calibration experiment, both the hot and cold inlet flows entered at the same temperature and heat loss was estimated as the sum of the enthalpy rates lost by both streams through the heat exchanger. Table 3 shows the results of heat loss experiments over the range of average UCS temperatures observed during heat transfer experiments. It is seen that over the range of average body temperatures between 55 and 90°C, the heat loss was relatively small, between 2 and 3 W, with no particular trend with body temperature. Based on the results of the heat loss experiment, a modified effectiveness was defined. The heat exchanger was split into two control volumes for heat loss modeling as shown in Fig. 6—one that lumped all the hot and

TABLE 3: Heat loss calibration experiment results

Average body temperature (°C)	Heat loss, $q_{\text{loss}} = q_{h,\text{loss}} + q_{c,\text{loss}}$ (W)
54.4	3.2
69.7	2.4
74.2	2.3
82.7	3.4
Average heat loss	2.8

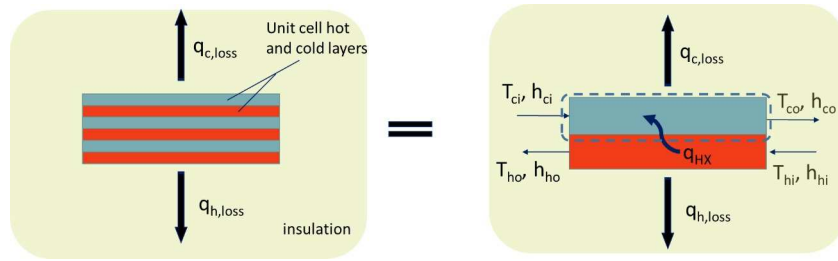


FIG. 6: Schematic of UCS with insulation (left) and a simplified representation for heat loss correction (right). The cold-side control volume is identified by the dashed rectangle.

cold layers together. Heat loss occurred on both the hot and cold sides ($q_{h,loss}$ and $q_{c,loss}$) and were assumed to be identical based on the heat loss calibration experiment. An energy balance was performed on the cold side control volume shown in Fig. 6 to yield

$$\dot{m}_c (h_{co} - h_{ci}) + q_{c,loss} = q_c + q_{c,loss} = q_{recup} \quad (7)$$

The estimated q_{recup} from Eq. (7) is then used to develop a modified estimate for effectiveness,

$$\varepsilon_{recup,mod} = (q_c + q_{c,loss}) / q_{max} \quad (8)$$

The modified heat rate on the cold side was used to estimate a modified estimate exit enthalpy and temperature of the cold side in the absence of heat loss. A similar energy balance was performed on the hot side to determine the modified exit enthalpy and temperature in the absence of heat loss. Together, these new exit temperatures were used to calculate a revised T_{lm} in the absence of heat loss using Eq. (6). Further, a revised NTU was estimated using Eqs. (5) and (4).

4.4 Experimental Results of UCS

In this section, experimental results of heat transfer and pressure drop of the UCS are presented. The overall heat transfer coefficient and pressure drop from experiments are compared with that obtained from correlations in literature on pin-fin arrays.

Figure 7 shows the heat transfer results in a non-dimensional form as effectiveness as a function of NTU defined by Eq. (4) for two nominal heat capacity rate ratios of 0.35 and 1. Two measures of effectiveness are plotted. The first is based on Eq. (1) and represents the heat loss uncorrected data and is shown in open symbols. The second is based on heat loss corrected data [Eq. (8)] and is represented as filled symbols. Note that the NTU values for the corrected data are different than the NTU calculated from Eq. (4) because of a change in the heat rate and log mean temperature difference due to heat loss corrections. At a C_r of 0.35, the effectiveness of the UCS was in excess of 90% for uncorrected data and 95% for heat-loss corrected data. At a larger C_r ranging from 0.84 to 1 (denoted for ease of visualization as $C_r = 1$ in Fig. 7), the effectiveness varied between 84 and 90% while the heat-loss corrected effectiveness ranged between 89 and 94%. Also plotted in Fig. 7 are trends for an ideal counter-flow heat exchanger for the two nominal C_r values of 0.35 and 1. It is clear that trend of ε -NTU for each tested C_r corresponds with the trend seen in standard counter-flow heat exchangers, with higher C_r data points exhibiting lower effectiveness at any given NTU.

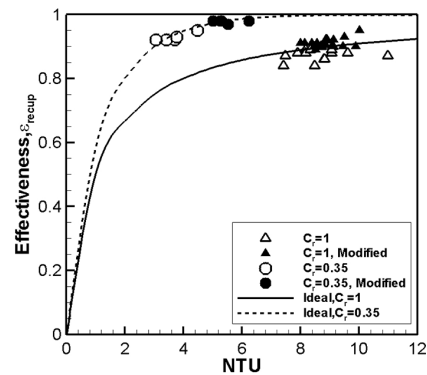


FIG. 7: UCS heat transfer results of effectiveness plotted against NTU. Legends represent approximate C_r for each test. Data were plotted against ideal trends seen in standard counter-flow heat exchangers at each C_r tested.

Another benchmark for judging the performance of the heat exchanger design is the effectiveness performance as a function of minimum approach temperatures, dT_{approach} . The minimum approach temperature for a counter-flow heat exchanger is defined as the smaller of either $dT_{\text{approach}} = T_{h,i} - T_{c,o}$ or $T_{h,o} - T_{c,i}$. In general, smaller approach temperatures result in higher effectiveness and cycle efficiency but also leads to a larger size of the heat exchanger. Figure 8 shows high effectiveness over a range of approach temperatures ranging from 5°C down to 1°C. There seems to be a slight increase in effectiveness with decrease in approach temperature for $C_r = 0.35$; however, no clear trend of effectiveness with dT_{approach} is observed for $C_r = 1$. Further experiments over a wider range of approach temperatures are needed to discern a clear trend.

Results of experimentally obtained U as a function of Re of the cold side can be seen in Fig. 9 in the open symbols. A near-linear increase in U from 300 to 950 W/m²-K with Re is observed in the range of Re from 850 to 2400. Note that the values of U in this work are significantly higher than that reported in literature (Nikitin et al., 2006; Tsuzuki et al., 2007) for the same Re . While a power-law relation would be expected for Nu as a function of Re in general, the near-linear increase is attributed to the small range in Re of the present study.

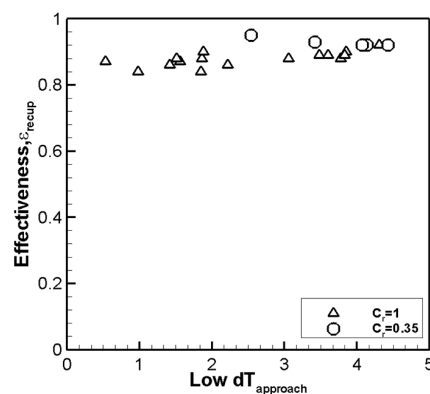


FIG. 8: Unit cell stack effectiveness as a function of minimum approach temperature

The experimentally determined U was compared against that predicted by pin-fin-array correlations in literature over the range of Re in the experiments. Table 4 summarizes the correlations in literature that are pertinent to this study. The range of validity of the correlations is also provided in Table 4. The correlation by Zukauskas (1972) was developed for cross-flow over a bank of tubes while the correlations by Short et al. (2002a), Prasher et al. (2007), and Rasouli et al. (2018) are based on flow through microscale pin arrays. The correlation by Short et al. (2002a) is based on air flow through millimeter-scale circular pin-fin arrays in a staggered configuration. Prasher et al. (2007) included the effects of pin geometry variations (circular vs. square) in their experiments on water flow through microscale pin-fin arrays. The correlation by Prasher et al. (2007) in Table 4 is a modified version of their original correlation that includes the effect of Prandtl number variation. They recommended this correction for comparing their experimental data, performed using water as the working fluid, with other correlations in literature. Rasouli et al. (2018) experimentally characterized heat transfer and pressure drop of single-phase liquid flow in eight micro-pin-fin arrays with varied pitch and aspect ratios. The pins were diamond shaped with respect to the flow. Nusselt number correlations were developed using two different fluids, PF-5060 and liquid nitrogen, to account for Prandtl number effects on heat transfer.

The predictions of the four correlations in Table 4 against experimentally derived U are shown in Fig. 9(b) for a C_r of unity. The mean absolute error (MAE) of the correlations, defined as

$$MAE = \frac{1}{N} \sum_1^N \frac{|\phi_{\text{exp}} - \phi_{\text{pred}}|}{\phi_{\text{exp}}} \times 100\% \quad (9)$$

is shown in the last column in Table 4. From Fig. 9(b) it is clear that none of the correlations match experimental U results well. The Prasher et al. (2007) correlation significantly over-predicts, while the Short et al. (2002a) correlation under-predicts, experimental U . The Zukauskas correlation over-predicts the experimental U by a smaller extent, with a MAE value

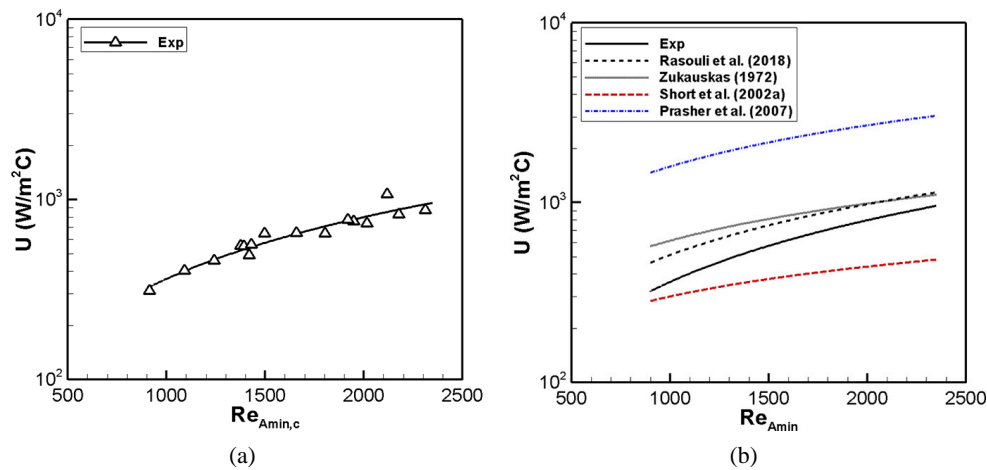


FIG. 9: Overall heat transfer coefficient of the unit cell stack (a) experimental results of overall heat transfer coefficient as a function of cold-side channel Reynolds number. (b) Comparison of experimental U with that determined using relevant correlations in literature. The solid black line is the curve fit of experimental data from (a).

TABLE 4: Correlations in literature on single-phase Nusselt number in pin-fin arrays

Reference	Remarks	Single-phase friction factor correlation	MAE%
Zukauskas (1972)	- Tube bank - Staggered circular tube - All fluids	$\text{Nu}_{Dh} = 0.35 (\beta_T / \beta_L)^{0.2} \text{Re}^{0.6} \text{Pr}^{0.36} (\text{Pr} / \text{Pr}_{\text{wall}})^{0.25}$ $1000 < \text{Re}_{Dh} < 2E5$ $\beta_T / \beta_L < 2 \quad \text{where} \quad \beta_T = S_T / D_h \quad \text{and} \quad \beta_L = S_L / D_h$	38.5
Short et al. [†] (2002a)	- Macro pin-fin heat sink - Staggered circular pin fin	$\text{Nu}_{Dh} = 0.419 \left(\frac{H}{D_h} \right)^{-0.3} \left(\frac{S_L}{D_h} \right)^{0.077} \left(\frac{S_T}{D_h} \right)^{0.2} \text{Re}^{0.45} \text{Pr}^{1/3}$ $\text{Re}_{Dh} > 1000,$ $1.9 < H_{\text{pin}} / D_h < 7.2$ $2.0 < S_T / D_h < 6.4$ $1.8 < S_L / D_h < 3.2$	36.1
Prasher et al. [‡] (2007)	- Micro pin-fin heat sink - Staggered circular and square pin fin	$\text{Nu}_{Dh} = 0.281 [(S_L - D_h) / D_h]^{-0.63} \text{Re}_{Dh}^{0.73} \left(\frac{\text{Pr}_{\text{test-fluid}}}{\text{Pr}_{\text{water}}} \right)^{0.36}$ $\text{Re}_{Dh} > 100$ $2.48 < H_{\text{pin}} / D_h < 2.8$ $2.4 < S_T / D_h = S_L / D_h < 3.6$	270.2
Rasouli et al. (2018)	- Micro pin-fin heat sink - Staggered diamond pin fin	$\text{Nu}_{Amin} = 0.039 [(S_T - D_h) / D_h]^{-0.19} \text{Re}_{Amin}^{0.837} \text{Pr}_{Amin}^{0.557}$ $40 < \text{Re}_{Amin} < 2300$ $0.7 < H_{\text{pin}} / D_h < 3.0$ $1.7 < S_T / D_h < 3.0$ $0.8 < S_L / D_h < 1.5$	29.0

[†]Short et al. (2002a) presented heat transfer data in Colburn j-factor, where $j = \text{Nu} / \text{RePr}^{1/3}$. The j correlations were converted to Nu_{Dh} based on this definition.

[‡]The authors' correlation does not have a Pr term. However, they used a Pr correction based on Zukauskas (1972), to compare their experimental data with literature. Based on the reported test conditions, water Pr was calculated at 52.5°C.

of 38.5%, with predictions getting better at higher Re . The Rasouli et al. (2018) correlation deviates from the experimental U the least, with an over-prediction by 29%. From Fig. 9(b), it is seen that the trend of experimental data is captured by this correlation. The heat loss uncorrected U values are compared in Fig. 9. If the heat loss corrected values were used, the MAE of the Rasouli et al. (2018) correlation would be 25%. Hence, the Rasouli et al. (2018) correlation is used in the heat exchanger model developed for cycle analysis in the next section.

From a comparison of pin array dimensions in Tables 1 and 4, it is clear that the aspect ratio and pitch ratio of the UCS pin array are out of the range of the correlations developed by Prasher et al. (2007) and Short et al. (2002a). Moreover, none of the correlations in Table 4 were developed for sCO_2 . While the Rasouli et al. (2018) correlation was developed with two different fluids with Pr in the range of 1.9 to 12.1, the Pr for sCO_2 in the experiment was lower and hence out of range of the correlation. It is clear that there is a need for additional experimental data with sCO_2 as the working fluid in microscale pin geometries, and at operating conditions seen in power cycles, to increase the predictive capability of the heat exchanger model.

The pressure drop (in kPa) across the fluid streams in the UCS is shown in Fig. 10(a). To obtain pressure drop data, flow was routed through only one side of the UCS (hot or cold) at a time in order to ensure a steady pressure drop measurement by isolating the channels of interest over a larger range of flow rates. The test was then repeated on the other set of channels. For testing, both channels were tested at the same fluid temperature, despite their hot/cold designation. Pressure drop in the range of 1.5–9 kPa was observed over the Re range from 800 to 4200. From Fig. 10(a), it can be seen that the pressure drop on both hot and cold flow sides of the heat exchanger match fairly well with each other. Also shown in Fig. 10(a) are results from CFD simulations at select Re . The CFD model was prescribed fluid properties and inlet mass flow rates consistent with conditions measured in the cold stream pressure drop tests. The comparison between the simulation and experimental pressure drop is good at Reynolds numbers under 3000 but the simulations seem to be over-predicting pressure drop at Re of ~ 3500 . The reason for the over-prediction by CFD at the highest Re is unclear.

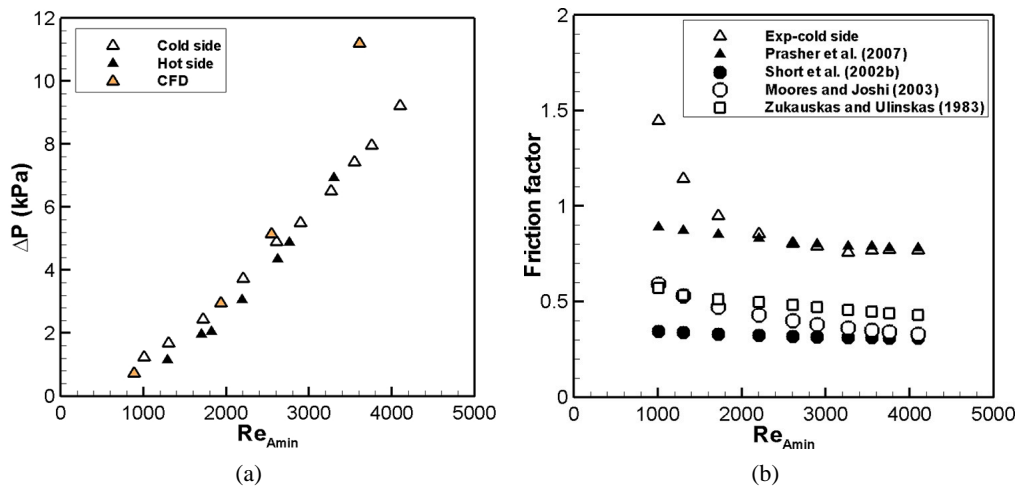


FIG. 10: Unit cell stack pressure drop results. (a) Adiabatic pressure drop measurements on both hot and cold sides of the unit cell stack. Also shown are CFD simulation pressure drop predictions. (b) Comparison of friction factor determined from experiments and from relevant correlations from literature.

Pertinent correlations in literature for predicting single-phase friction factor on micro pin-fin heat sinks are listed in Table 5. The correlations were selected based on the closest match of the pin-fin pitch and aspect ratios range between the present study and that for which the correlations had been developed. The Prasher et al. (2007) correlation was developed based on testing of three heat sinks with circular pin fins. The authors performed pressure drop testing on two square μ PFHS as well. The correlation of Short et al. (2002b) was developed based on a comprehensive study on friction factor of macroscale pin-fin heat sinks with air flow. The observed change in the slope of f - Re_{Dh} curves made the author correlate their data with two correlations for $Re_{Dh} < 1000$ proportional to $Re_{Dh}^{-0.65}$ and for higher Reynolds numbers with $Re_{Dh}^{-0.08}$. Moores and Joshi (2003) correlated their experimental friction factor data of water flow across mesoscale pin-fin heat sinks with and without a clearance between tip of the pin fins and heat sink's top wall. The Zukauskas correlation (Zukauskas and Ulinskas, 1983) was based on cross flow through a bank of staggered tubes.

The comparison of the correlations in Table 5 with experimental data is shown in Fig. 10(b). The MAE of prediction is also noted in Table 5. From Fig. 10(b), it is clear that the Zukauskas and Ulinskas (1983), Short et al. (2002b), and Moores and Joshi (2003) correlations underpredict the experimental pressure drop. The Prasher et al. (2007) correlation predicts the experimental data to within 9%. For Re larger than 2000, the match between the correlation and experimental data is excellent. Hence, this correlation is selected for use in the heat exchanger model described in the next section.

5. UNIT CELL HEAT EXCHANGER-PRELIMINARY THERMOFLUIDIC MODEL

In order to develop a simplified thermo-fluidic model for a full-scale IHM recuperator, two aspects need to be incorporated in a design model: (1) a validated unit cell heat exchanger model, and (2) header and plenum design to ensure uniform flow distribution into each unit cell (see Fig. 1). The latter is achieved using CFD simulations of fluid flow through headers and does not affect heat transfer or pressure drop significantly since the flow dimensions in the headers are larger than through the unit cells. In this section, a design model for heat exchange within a unit cell of the microchannel recuperator is presented. The output of the model is the heat exchanger size for given input flow conditions based on dimensions of the microscale flow passages.

The unit cell was modeled using ε -NTU relationship for a counter-flow heat exchanger (Bergman et al., 2011). Classical assumptions including negligible heat loss to the environment, constant properties, and negligible axial conduction were used. Axial conduction was verified to be negligible based on the dimensions of the unit cell stack in the range of experimental conditions. Based on given pin array dimensions and mass flow rate through the unit cell, the overall heat transfer coefficient for NTU was determined using the Rasouli et al. (2018) pin-fin array heat transfer correlation from the prior section. Based on a set effectiveness from the cycle model (see the next section), the unit cell dimensions could be calculated using the unit cell heat exchanger model. The Prasher et al. (2007) correlation was then used to determine the pressure drop through the unit cell.

Since various geometrical and flow parameters can be varied, some of the variables were kept fixed to provide sizing estimates in the cycle analysis presented in the next section. The width of each unit cell was fixed at $W_{\text{unit cell}}$ of 1 m and the wall thickness (t_{wall}) between the hot and cold streams was fixed at 500 μm . The computed unit cell length ($L_{\text{unit cell}}$) along with the specified width ($W_{\text{unit cell}}$) were used along and the fluid stream channel heights (H_c and H_h) to

TABLE 5: Literature correlations for single-phase friction factor in pin-fin arrays

Reference	Remarks	Single-phase friction factor correlation	MAE%
Prasher et al. (2007)	- Micro pin-fin heat sink - Staggered circular and square pin fin	$f = 4 * 0.295 \left(\frac{H}{D_h} \right)^{1.249} \left(\frac{S_L - D_h}{D_h} \right)^{-0.7} \left(\frac{S_T - D_h}{D_h} \right)^{-0.36} \text{Re}^{-0.1}$ $\text{Re}_{D_h} > 100$ $1.3 < H_{\text{pin}}/D_h < 2.8$ $2 < S_T/D_h < 3.6$ $2.4 < S_L/D_h < 4$	8.9
Short et al. [†] (2002b)	- Macro pin fin heat sink - Staggered circular pin fin	$f = 4 * 0.221 \left(\frac{H}{D_h} \right)^{-0.056} \left(\frac{S_L}{D_h} \right)^{-1.4} \left(\frac{S_T}{D_h} \right)^{-0.54} \text{Re}^{-0.08} \left(\frac{L}{D_h N_{row}} \right)$ $\text{Re}_{D_h} > 1000,$ $1.9 < H_{\text{pin}}/D_h < 7.2$ $2.0 < S_T/D_h < 6.4$ $1.8 < S_L/D_h < 3.2$	63.3
Moore and Joshi (2003)	- Meso pin-fin heat sink - Staggered circular pin fin	$f = 4 * 3.2 (H/D_h)^{-0.138} \text{Re}^{-0.42}$ $1000 < \text{Re}_{D_h} < 10000,$ $0.5 < H_{\text{pin}}/D_h < 1.1$ $1.3 < S_T/D_h < 1.36$ $1.13 < S_L/D_h < 1.18$	53.6
Zukauskas and Ulinskas (1983)	- Tube bank - Staggered circular tube - All fluids	$f = 0.203 + 0.248E4\text{Re}^{-1} - 0.758E7\text{Re}^{-2} + 0.104E11\text{Re}^{-3} - 0.482E13\text{Re}^{-4}$ $1000 < \text{Re}_{D_h} < 2E6$ $S_T/D_h = 1.5$ $S_T/S_L = 1.25$	45.2

[†]The factor of $L/D_h N_{row}$ was applied because of the difference in the definition of f used by Short et al. (2002b) with this study.

determine a unit cell volume,

$$V_{\text{unit cell}} = 1.25 \times L_{\text{unit cell}} \times W_{\text{unit cell}} \times (H_h + H_c + 2 \times t_{\text{wall}}) \quad (10)$$

The unit cell volume was increased by 25% to include space for the flow distribution regions within the unit cell (see Figs. 1 and 3). Based on the unit cell volume, a preliminary estimate of the total volume of the IHM recuperator was determined as

$$V_{\text{IHM}} = 1.5 \times V_{\text{unit cell}} \times N_{\text{unit cells in stack}} \times N_{\text{stacks}} \quad (11)$$

where $N_{\text{unit cells in stack}}$ refers to the number of unit cells in a stack and N_{stacks} refers to the number of stacks containing $N_{\text{unit cells in stack}}$ of unit cells each (see Fig. 1). A factor of 50% is to account for the integrated flow distribution plena shown in Fig. 1. Since the actual fluid volume is about 23% of the unit cell volume for the UCS design, the size of the plenum is about two times the entire volume of fluid in the unit cells. Hence, the velocity of flow within the plenum would be significantly lower than that within the pin arrays in the unit cells, lending to a uniform flow distribution across the unit cells. A more detailed design is needed in the future to determine the exact size of the integrated plena. Additionally, the detailed model should include sectional analysis of the recuperator in order to account for varying thermo-physical properties.

6. CYCLE IMPLICATIONS OF USING THE IHM RECUPERATOR

The simplified correlation-based unit cell design model developed in the prior section was integrated into a cycle-level thermodynamic model to determine the impact of recuperator design on the cycle efficiency. A single-stage recuperator sCO₂ power cycle was modeled. The purpose of this analysis is to provide perspective on the impact of the proposed recuperator design on the cycle efficiency.

The T-s diagram of the cycle is shown in Fig. 11. A schematic of the components in sCO₂ power generation cycle with the corresponding state points is shown in the inset schematic. There are six operating steps: 1-2 isentropic compression (compressor, pressure increase to 200 bar), 2-3 isobaric heat input (recuperator), 3-4 isobaric heat input (primary heat exchanger), 4-5 isentropic expansion (turbine, pressure decrease down to 80 bar), 5-6 isobaric heat removal (recuperator), and 6-1 isobaric heat removal (heat rejection heat exchanger).

To evaluate the impact of recuperator effectiveness (ϵ_{recup}) and the design on the overall power generation cycle efficiency (η), the unit cell recuperator model described in the prior section was incorporated into a thermodynamic model developed for a brayton sCO₂ cycle with a single recuperator. The cycle was modeled in Engineering Equation Solver software (F-Chart inc.).

Figure 12 shows a flow diagram of the coupled cycle-recuperator model. the variables in Fig. 12 correspond to the state points in Fig. 1. The cold sCO₂ inlet and exit state points for the recuperator were 2 and 3, respectively, while the hot sCO₂ inlet and exit state points were 5 and 6, respectively. The high pressure of the cycle P_2 was defined to be 200 bar and the low pressure P_5 was defined to be 80 bar. Inefficiencies of the turbine and compressor were not considered. The mass flow rate of sCO₂ through the closed cycle was kept fixed at 200 kg/s. the capacity of the recuperator varied depending on the effectiveness of the IHM recuperator. The number of unit cell stacks and the number of unit cells per stack were determined based on maintaining a Re in each unit cell hot and cold flow streams in the range of the UCS experimental data. Depending on the average fluid temperature in the unit cell, the hot-side Re varied between 1620 to 1930,

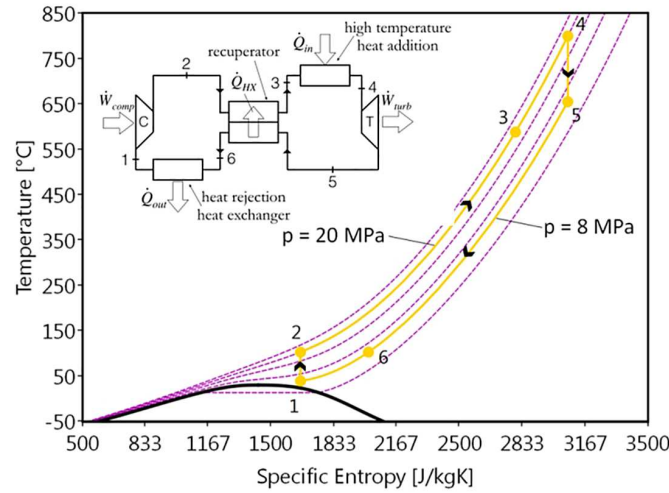


FIG. 11: Temperature-specific entropy diagram of a single recuperation sCO₂ cycle. A schematic of the components is shown in the inset figure.

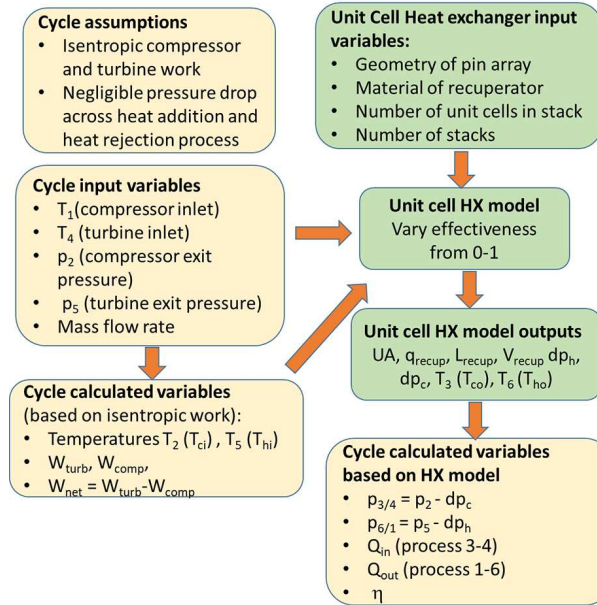


FIG. 12: Flow diagram for combined cycle and recuperator model

while the cold-side Re varied between 1884 and 2049. The arrangement of the IHM recuperator consisted of nine stacks of 1000 unit cells in each stack (see Fig. 1) for a total of 9000 unit cells.

Based on a prescribed effectiveness of the recuperator, the unit cell length and pressure drop was calculated from the unit cell heat exchanger model. The unit cell volume and recuperator volume was estimated using Eqs. (10) and (11), respectively. The pressure drop from the recuperator model was then fed into the cycle-level model to determine the impact of pressure drop

on the cycle performance. Table 6 shows values at which input parameters identified in Fig. 12 were held fixed for the results shown in this section. The upper limit of T_4 of 800°C was based on component constraints such as the temperature limits of materials used in the turbine. The pin array dimensions were kept identical to the ones used in the experiments (Table 1).

The effect of the recuperator effectiveness, $\varepsilon_{\text{recup}}$, on the efficiency of the cycle is shown in Fig. 13(a). From Fig. 13(a), it can be seen that recuperator effectiveness has a significant impact on the cycle efficiency; having high values of $\varepsilon_{\text{recup}}$ is hence important in order to achieve a reasonable cycle efficiency. The steep increase of η with increasing $\varepsilon_{\text{recup}}$, especially in the range of $0.8 \leq \varepsilon_{\text{recup}} \leq 1$ is especially noticeable, indicating that significant gains in cycle efficiency can be obtained by increasing the recuperator effectiveness in this range. For example, increasing the recuperator effectiveness from 90% to 95% percent increases the cycle efficiency from 43.5% to 48%. Such increase in cycle efficiency at high recuperator effectiveness comes with lower approach temperature across the recuperator.

The variation of minimum approach temperature difference in the recuperator as a function of recuperator effectiveness is shown on the secondary ordinate in Fig. 13(a). As described in conjunction with Fig. 9, the approach temperature difference can exist on either side of the recuperator and can be calculated from $T_{h,i} - T_{c,o}$ or $T_{h,o} - T_{c,i}$. From Fig. 13(a), it is clear that approach temperatures of under 20°C are observed for recuperator effectiveness in excess of 95%. As seen in Fig. 9, the UCS experiments indicate that high effectiveness is achieved over the range of approach temperatures in the experiments between 1°C and 5°C, indicating the viability of the UCS design for this application.

TABLE 6: Values of input variables for the integrated cycle-recuperator model

Cycle fixed variables	Assigned values
Turbine inlet temperature, T_4 (°C)	800
Compressor inlet temperature, T_1 (°C)	40
Compressor outlet pressure P_2 (bar)	200
Turbine exit pressure, P_5 (bar)	80
sCO ₂ mass flow rate (kg/s)	200
Recuperator model fixed variables	
Recuperator material	IN718
Unit cell width, $W_{\text{unit cell}}$ (m)	1
Wall thickness between hot and cold sides (μm)	500
Pin diameter (μm)	797
Pin array height (μm)	500
Pin array transverse pitch, S_T (μm)	1186
Pin array longitudinal pitch, S_L (μm)	1054
Number of unit cells in a stack, $N_{\text{unit cells in stack}}$	1000
Number of stacks, N_{stack}	9
$\text{Re}_{Amin,h}$	1620–1930
$\text{Re}_{Amin,c}$	1884–2049

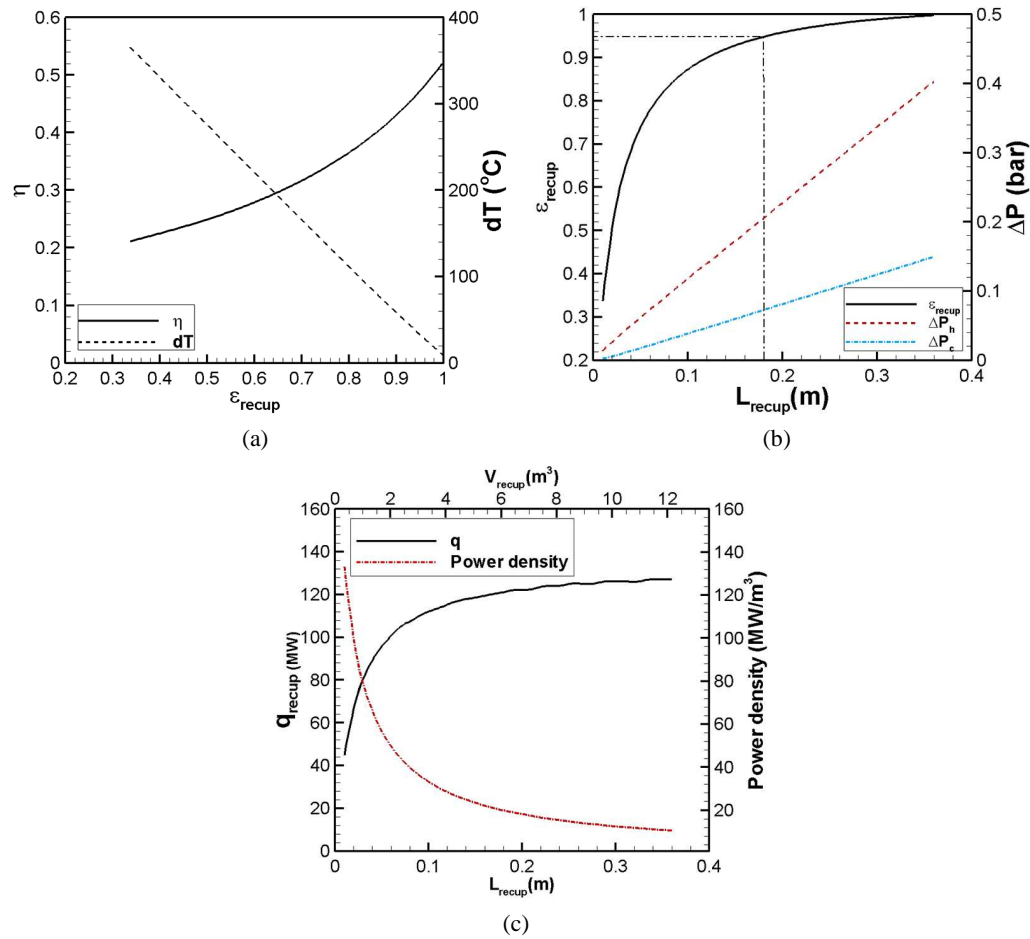


FIG. 13: Results from the integrated cycle-IHM recuperator model. (a) Variation of cycle efficiency and minimal temperature difference as a function of recuperator effectiveness. (b) Recuperator effectiveness and hot- and cold-side pressure drop as a function of recuperator length. (c) Heat exchange rate and power density trends plotted against the length and volume of the recuperator.

One way to increase the recuperator effectiveness is by increasing the length of the recuperator. However, this increase in length would result in a pressure drop penalty. The effect of recuperator unit cell length on effectiveness and pressure drop is shown in Fig. 13(b). Note that since the width and pin array dimensions are fixed, an increase in length of the recuperator would correspond to an increase in volume. The recuperator inlet fluid temperatures, $T_{h,i}$ and $T_{c,i}$ were estimated quantities but were around 656°C and 110°C, respectively. It is seen in Fig. 13(b) that the length of the recuperator strongly affects the effectiveness and pressure drop across the recuperator. At a length of 18 cm [see dashed-dotted line in Fig. 13(b)], which was identical to that used in the UCS experiments, an effectiveness of ~ 95 is obtained. Higher effectiveness can be achieved with trade-off in larger pressure drop and capital cost. The pressure drop on the hot side (ΔP_h) is markedly higher than that of the cold side due to the density variation of sCO₂ ($P_h = 80$ bar vs. $P_c = 200$ bar). The large pressure drop on the hot side can be reduced by

increasing the height of the pin array on this side of the heat exchanger. However, in order to do so, a more expensive manufacturing process, such as sinker electric discharge machining, would need to be employed. Such modifications to the fabrication process are not crucial in the IHM design since the shorter unit cell length ensures that the pressure drop is low. For example, the pressure drop is less than 0.25 bar for both cold and hot sides at a length of 18 cm.

The capacity and power density of the IHM recuperator are plotted as a function of recuperator length and volume in Fig. 13(c). For a fixed mass flow rate of 200 kg/s, recuperator capacity of greater 120 MW can be attained at a unit cell length of 18 cm. The energy density of the recuperator is high for small lengths of the unit cell but decreases to an asymptote with larger lengths. However, the large energy density at smaller lengths is due to the smaller volume and not increased capacity. At a unit cell length of 18 cm, a power density of 20 MW/m³ can be obtained. Note that the sizing estimates are based on scaled factors for the headers and plena and more detailed analysis of the headers and plena are needed to obtain more accurate estimates of the IHM recuperator size. However, the preliminary estimates provided in this section show the promise of a recuperator design with integrated branched plenum architecture.

7. CONCLUSIONS

Design of a microscale recuperator with integrated header architecture for a sCO₂ power cycle was presented. The recuperator consisted of multiple unit cells of microscale flow passages coupled together using headers and plena. A three-layer microscale pin-fin UCS was designed, fabricated, and experimentally characterized. Overall heat transfer coefficients and pressure drop derived from the experimental results were compared with those obtained from literature. A correlation-based recuperator model was developed and integrated into a thermodynamic model to determine the effect of varying geometrical parameters of the IHM recuperator on the cycle efficiency.

Salient results are summarized below:

- High effectiveness over a range of approach temperatures and heat capacity rate ratios, C_r , was achieved experimentally. For $C_r \sim 1$, the heat loss uncorrected effectiveness ranged from 84% to 90% while for a $C_r \sim 0.35$, the effectiveness ranged between 90% and 95%.
- Overall heat transfer coefficients in the range of 300–1000 W/m²-K were obtained at reynolds numbers range of 900–2400. The U values in this work are significantly larger than that reported in literature for the same range of Re.
- Experimental pressure drop measurements compared well with CFD results for Re less than 2400. Pressure drop correlation by Prasher et al. (2007) predicted the experimental values with an mae of less than 9%. The match between experimental and Prasher et al. (2007) correlation pressure drop is excellent at Re > 2000.
- None of the heat transfer correlations developed for pin-fin arrays predicted experimentally derived overall heat transfer coefficient with reasonable errors. The best match, both in trend and least MAE (29%), was obtained using the correlation by Rasouli et al. (2018). There is hence a need for a correlation for sCO₂ flows through such pin arrays in order to obtain better predictive capabilities of heat exchange models.

- The integrated recuperator and cycle model highlights the importance of a short unit cell design of the IHM architecture. A unit cell length of 18 cm provides an effectiveness of 95% with pressure drops under 0.25 bar on both hot and cold sides of the unit cell.
- Preliminary estimates of IHM recuperator size were provided based on assumptions of header size as a fraction of the unit cell stack volume. The results indicate that power densities on the order of 20 MW/m^3 can be achieved using the IHM architecture. A more detailed analysis of headering and flow distribution within the headers is warranted to obtain a better estimate.

ACKNOWLEDGMENTS

Financial support for this work was provided by federal grant DE-FE0024064 from the Fossil Energy Office of the Department of Energy. The views and opinions of authors expressed herein do not necessarily state or reflect those of the United States Government or any agency thereof.

REFERENCES

- Ahn, Y., Bae, S.J., Kim, M., Cho, S.K., Baik, S., Lee, J.I., and Cha, J.E., Review of Supercritical CO_2 Power Cycle Technology and Current Status of Research and Development, *Nucl. Eng. Technol.*, vol. **47**, pp. 647–661, 2015.
- American Iron and Steel Institute (AISI), High Temperature Characteristics of Stainless Steels, A Designer's Handbook Series No. 9004, accessed July 26, 2018, from https://www.nickelinstitute.org/en/TechnicalLibrary/AISI/9004_High_TemperatureCharacteristicsOfStainlessSteel.aspx, 2018.
- Bergman, T.L., Lavine, A.S., Incropera, F.P., and DeWitt, D.P., *Fundamentals of Heat and Mass Transfer*, 7th ed., Hoboken, NJ: John Wiley and Sons, 2011.
- Brandner, J., Bohn, L., Henning, T., Schygulla, U., and Schubert, K., Microstructure Heat Exchanger Applications in Laboratory and Industry, *Heat Transf. Eng.*, vol. **28**, pp. 761–771, 2007.
- Brun, K., Friedman, P., and Dennis, R., Eds., *Fundamentals and Applications of Supercritical Carbon Dioxide (sCO_2) Based Power Cycles*, 1st ed., UK: Woodhead Publishing, 2017.
- Carlson, M.D., Kruienga, A.K., Schalansky, C., and Fleming, D.F., Sandia Progress on Advanced Heat Exchangers for sCO_2 Brayton Cycles, *Proc. of the 4th Intl. Symp. on Supercritical CO_2 Power Cycles*, Pittsburgh, PA, September 9–10, 2014.
- Chen, M., Sun, X., Christensen, R.N., Skavdahl, I., Utgikar, V., and Sabharwall, P., Pressure Drop and Heat Transfer Characteristics of a High Temperature Printed Circuit Heat Exchanger, *Appl. Therm. Eng.*, vol. **108**, pp. 1409–1417, 2016.
- Fourspring, P.M., Nehrbauer, J.P., Sullivan, S., and Nash, J., Testing of Compact Recuperators for a Supercritical CO_2 Brayton Power Cycle, *Proc. of the 4th Intl. Symp. on Supercritical CO_2 Power Cycles*, Pittsburgh, PA, September 9–10, 2014.
- Irwin, L. and Moullec, Y.L., Turbines Can Use CO_2 to Cut CO_2 , *Science*, vol. **356**, no. 6340, pp. 805–806, 2017.
- Karagiannidis, S. and Mantzaras, J., Numerical Investigation on the Start-Up of Methane-Fueled Catalytic Microreactors, *Combust. Flame*, vol. **157**, pp. 1400–1413, 2010.
- Kim, H. and No, C., Thermal Hydraulic Performance Analysis of a Printed Circuit Heat Exchanger Using a Helium-Water Test Loop and Numerical Simulations, *Appl. Therm. Eng.*, vol. **31**, pp. 4064–4073, 2011.
- Kockmann, N., *Transport Phenomena in MicroProcess Engineering*, Berlin, Germany: Springer Publishing Group, 2008.

- Le Pierres, R., Southall, D., and Osborne, S., Impact of Mechanical Design on Printed Circuit Heat Exchangers, *Proc. of the 2011 SCO₂ Power Cycle Symp.*, University of Colorado Boulder, May 24–25, 2011.
- Li, X., Le Pierres, R., and Dewson, S.J., Heat Exchangers for the Next Generation of Nuclear Reactors, Paper 6105, *Proc. ICAPP 2006*, Reno, NV, 2006.
- Li, X., Kinninmont, D., Le Pierres, R., and Dewson, S.J., Alloy 617 for the High Temperature Diffusion-bonded Compact Heat Exchangers, Paper 8008, *Proc. ICAPP 2008*, Anaheim, CA, USA, June 8–12, 2008.
- Meshram, A., Jaiswal, A.K., Khivsara, S.D., Ortega, J.D., Ho, C., Bapat, R., and Dutta, P., Modeling and Analysis of a Printed Circuit Heat Exchanger for Supercritical CO₂ Power Cycle Applications, *Appl. Therm. Eng.*, vol. **109**, pp. 861–870, 2016.
- Moffat, R., Describing the Uncertainties in Experimental Results, *Exp. Therm. Fluid Sci.*, vol. **1**, no. 1, pp. 3–17, 1988.
- Moore, K.A. and Joshi, Y.K., Effect of Tip Clearance on the Thermal and Hydrodynamic Performance of a Shrouded Pin Fin Array, *J. Heat Transf.*, vol. **125**, no. 6, pp. 999–1006, 2003.
- Mylavarapu, S.K., Sun, X., Christensen, R.N., Unocic, R.R., Glosup, R.E., and Patterson, M.W., Fabrication and Design Aspects of High-temperature Compact Diffusion Bonded Heat Exchangers, *Nucl. Eng. Des.*, vol. **249**, pp. 49–56, 2012.
- Naderi, C., Experimental Study of Micro Pin-Fin Heat Sinks and Supercritical Carbon Dioxide Microchannel Heat Exchanger, MS, University of California Davis, 2017.
- Narayanan, V., Liburdy, J., and Pence, D., Thermal Applications of Microchannel Flows, in *Encyclopedia of Aerospace Engineering*, R. Blockley and W. Shyy, Eds., Chichester, UK: John Wiley, 2013.
- Ngo, T.L., Kato, Y., Nikitin, K., and Ishizuka, T., Heat Transfer and Pressure Drop Correlations of Microchannel Heat Exchangers with S-Shaped and Zig-Zag Fins for Carbon Dioxide Cycles, *Exp. Therm. Fluid Sci.*, vol. **32**, pp. 560–570, 2007.
- Nikitin, K., Kato, Y., and Ngo, L., Printed Circuit Heat Exchanger Thermal-Hydraulic Performance in Supercritical CO₂ Experimental Loop, *Int. J. Refrig.*, vol. **29**, pp. 807–814, 2006.
- Peles, Y., Koşar, A., Mishra, C., Kuo, C.J., and Schneider, B., Forced Convective Heat Transfer across a Pin Fin Micro Heat Sink, *Int. J. Heat Mass Transf.*, vol. **48**, no. 17, pp. 3615–3627, 2005.
- Prasher, R.S., Dirner, J., Chang, J.Y., Myers, Chau, A.D., He, D., and Prstic, S., Nusselt Number and Friction Factor of Staggered Arrays of Low Aspect Micropin-Fins under Cross Flow for Water as Fluid, *J. Heat Transf.*, vol. **129**, no. 2, pp. 141–153, 2007.
- Rasouli, E., Naderi, C., and Narayanan, V., Pitch and Aspect Ratios Effects on Single-Phase Heat Transfer through Microscale Pin Fin Heat Sinks, *Int. J. Heat Mass Transf.*, vol. **118**, pp. 416–428, 2018.
- Short, B.E., Raad, P.E., and Price, D.C., Performance of Pin Fin Cast Aluminum Cold Walls. Part 2: Colburn J-Factor Correlations, *Thermophys. Heat Transf.*, vol. **16**, pp. 397–403, 2002a.
- Short, B.E., Raad, P.E., and Price, D.C., Performance of Pin Fin Cast Aluminum Cold Walls, Part. 1: Friction Factor Correlations, *J. Thermophys. Heat Transf.*, vol. **16**, no. 3, pp. 389–396, 2002b.
- Tonkovich, A.Y., Perry, S., Wang, Y., Qiu, D., LaPlante, T., and Rogers, W.A., Microchannel Process Technology for Compact Methane Steam Reforming, *Chem. Eng. Sci.*, vol. **59**, pp. 4819–4824, 2004.
- Tsuzuki, N., Kato, Y., and Ishiduka, T., High Performance Printed Circuit Heat Exchanger, *Appl. Therm. Eng.*, vol. **27**, pp. 1702–1707, 2007.
- Tuckerman, D.B., Heat-Transfer Microstructures for Integrated Circuits, PhD, Stanford University, CA, 1984.
- Tuckerman, D.B. and Pease, R.F.W., High-Performance Heat Sinking for VLSI, *IEEE Electron Devices*

- Lett.*, vol. **EDL-2**, no. 5, pp. 126–129, 1981.
- Turchi, C.S., Ma, Z., Neises, T.W., and Wagner, M.J., Thermodynamic Study of Advanced Supercritical Carbon Dioxide Power Cycles for Concentrating Solar Power Systems, *J. Solar Energy Eng.*, vol. **135**, paper 041007-1, 2013.
- Zukauskas, A., Heat Transfer from Tubes in Crossflow, *Adv. Heat Transf.* vol. **8**, New York: Academic, pp. 93–160, 1972.
- Zukauskas, A. and Ulinskas, R., Single-Phase Fluid Flow: Banks of Plain and Finned Tubes, in *Heat Exchanger Design Handbook*, E.U. Schlunder, Eds., New York: Washington Hemisphere Publishing, Chap. 2.2.4, 1983.